ACS APPLIED MATERIALS & INTERFACES
Research Article
www.acsami.org

Monodisperse Aluminosilicate Spheres with Tunable Al/Si Ratio and Hierarchical Macro-Meso-Microporous Structure

Yuan Sheng[†] and Hua Chun Zeng*[,†,‡]

[†]Department of Chemical and Biomolecular Engineering, National University of Singapore, 10 Kent Ridge Crescent, Singapore 119260

[‡]Institute of Materials Research and Engineering (IMRE), 3 Research Link, Singapore 117602

Supporting Information

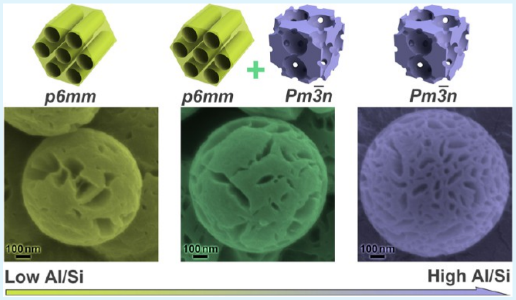

ABSTRACT: While tremendous success has been seen in the development of ordered mesoporous silica by soft-templated methods, synthesis of hierarchical structures with controllable multiscale pore networks has remained a challenging topic. On the other hand, introduction of heteroatoms as an effective method of chemically functionalizing silica leads to difficulties in morphological control of the product, and multistep synthesis has been necessary for functionalized silica particles with hierarchical pore structure and uniform size. The present work demonstrates that the conflict between morphological control and heteroatom incorporation can be resolved in a CTAB-stabilized toluene−water−ethanol microemulsion system. For the first time, monodisperse macro-meso-microporous aluminosilicate spheres (MASS) are synthesized in one step at room temperature. Simultaneous tuning of Al/Si ratio (0−0.35) and the hierarchical pore structure is realized by Hofmeister anion effects of the Al source itself, $[\mathrm{Al(OH)_4}]^-$, which change the geometry of CTAB micelles and giant vesicles. The Al is incorporated purely in a tetrahedrally coordinated status, and preliminary results from catalytic experiments show improved acidity of MASS as a catalyst support.

KEYWORDS: *hierarchical structures, aluminosilicates, mesoporous materials, microemulsion, Hofmeister anion effects*

1. INTRODUCTION

Mesoporous silicate molecular sieves have gained increasing interest ever since the first synthesis of MCM-41.[1,2] The large surface area and chemical inertness make this class of materials useful in separation,[3] drug delivery,[4] and heterogeneous catalysis.[5] In a comparison with the crystalline structure of zeolites and metal−organic frameworks, the amorphous nature of mesoporous silica offers more flexibility in terms of structural tuning which is essential in the synthesis of complex, multifunctional materials.[6] In addition, the lower diffusion barrier of mesoporous structures allows for more efficient utilization of internal surface areas and higher resistance toward pore plugging.[7] With early works emerging in the 1990s,[8] the synthesis of hierarchically macro-mesoporous silica has been frequently reported recently,[4,9−12] illustrating well the versatility of amorphous siliceous materials. The interconnected mesopores and macropores of such materials lead to high accessibility of internal surfaces and provide enough space for integration with bulk phases that is impossible in solely mesoporous materials.[13] However, a majority of industrially important catalytic reactions involve molecular species sized below the mesoporous range, and to really explore the molecular sieving properties of porous silica, microporous structures are required.[14] Although it seems probable to tackle the conflict between pore accessibility and size selectivity by integrating microporous and mesoporous materials,[15,16] a more facile single-step approach is still preferred where hierarchical macro-meso-microporous structures can form simultaneously. Unfortunately, no such works on aluminosilicate materials have been reported so far.

On the other hand, purely siliceous materials lack reactive sites, and their functionalization relies entirely on incorporation of heteroatoms. In particular, Al is frequently introduced to create acidic sites in porous silica.[17−29] It has been shown that the acidity of the resultant aluminosilicate is closely related to the coordination environment of incorporated Al which in turn depends on the chemistry of precursor solution.[19,21−23,25,30] Tetrahedrally coordinated Al is capable of producing stronger acid sites than its octahedral counterpart, and to introduce Al as tetrahedral complexes an alkaline environment is beneficial due to the following equilibria,[31,32] where Roman numeral superscripts denote the coordination number of Al:

$$[\mathrm{Al^{VI}(H_2O)_6}]^{3+} + 3\mathrm{OH^-} \leftrightarrow \mathrm{Al^{VI}(OH)_3}\cdot n\mathrm{H_2O} + (6-n)\mathrm{H_2O} \qquad (1)$$

$$\mathrm{Al^{VI}(OH)_3}\cdot n\mathrm{H_2O} + \mathrm{OH^-} \leftrightarrow [\mathrm{Al^{IV}(OH)_4}]^- + n\mathrm{H_2O} \qquad (2)$$

Received: April 7, 2015
Accepted: June 2, 2015
Published: June 2, 2015

DOI: 10.1021/acsami.5b03011

However, direct introduction of Al compounds into the precursor solution poses negative effects on the morphological control of the aluminosilicate material. Unlike mesoporous silica particles which have been prepared with well-defined shape and sizes,[33] aluminosilicate was usually obtained in the form of nonuniform particles[7,17,23] or macroscopic aggregates.[24,25,29] Attempts have been made to resolve the issue by a two-step approach whereby morphologically well-defined SiO_2 particles were first synthesized and then grafted with Al through hydrothermal processing,[28] but the relatively complicated synthetic procedure is a significant drawback. For practical purposes, the single-step approach is much more desired.

During the development of synthetic strategies of mesoporous silica, the nature of ionic species present in the precursor mixture have been found to strongly influence the pore structure of the product, especially for the combination of anions and cationic surfactant templates.[29,34,35] Such effects are often referred to as Hofmeister anion effects, a term derived from Hofmeister's work on solubilization of proteins by different salts.[36] Briefly, anions are ordered in the "Hofmeister series" according to increasing potency of solubilizing proteins as follows:[37]

$$SO_4^{2-} < OH^- < F^- < Cl^- < Br^- < NO_3^- < I^-$$

According to general understanding,[37,38] the solubilizing power is related to the polarizability and hydration structure-forming (cosmotropic) or -breaking (chaotropic) tendencies of the anions; those to the left of Cl^- or "cosmotropic ions" form strongly bound hydrated structures and exhibit weaker charge screening effects on surfactant micelles than ions to the right of Cl^- or "chaotropic ions". With the adsorption of cosmotropic ions, the effective charge of cationic surfactant micelles increases. The increased charge generates stronger repulsive Coulomb force and hence longer equilibrium distance between surfactant head groups in an individual micelle,[39] which in turn reduces the surfactant packing parameter,[35,40] $g = V/(a_0 l)$ where V is the effective volume of hydrophobic part of the surfactant, a_0 is the effective area of surfactant headgroup at the micelle surface, and l is the kinetic length of the hydrophobic tail. Consequently, the spontaneous assembling of surfactant molecules into surfaces with high curvature is favored. In addition, intermicellar repulsion is also increased, preventing the coalescence of micelles. In fact, not only micelles but also liquid droplets in surfactant-stabilized emulsions experience similar effects.[41,42] So far remarkable success has been seen in applying Hofmeister anion effects to materials synthesis,[29,34,35,43] but research on this topic has been largely limited to nonmetal anions (e.g., Cl^-, NO_3^-, SO_4^{2-}, etc.) in mesoscopic systems. Recently, a study on the assembly of noble metal clusters and cetyltrimethylammonium bromide (CTAB) micelles showed profound morphological effects of the metal precursors, i.e., $[AuCl_4]^-$, $[PtCl_4]^-$, and $[PdCl_4]^-$,[44] which is actually an example of Hofmeister anion effects (class II ions which have large polarizabilities).[37] In the present work, the generality of Hofmeister anion effects is further demonstrated by controlled synthesis of macro-meso-microporous aluminosilicate spheres (MASS) in a microemulsion system. The microemulsion containing both nanosized surfactant micelles and submicron giant vesicles serves as an ideal platform for the exploitation of the multiscale Hofmeister anion effects of $[Al(OH)_4]^-$, and provides crucial morphological control during the incorporation of Al, which leads to monodispersity of MASS.

2. EXPERIMENTAL SECTION

2.1. Chemicals. Cetyltrimethylammonium bromide (CTAB, 96%), tetraethyl orthosilicate (TEOS, 99%), zinc nitrate ($Zn(NO_3)_2 \cdot 6H_2O$, 99%), and ethylenediamine (EDA, 99.5%) were purchased from Sigma-Aldrich. Copper(II) nitrate ($Cu(NO_3)_2 \cdot 3H_2O$, 99.5%), ammonia solution (NH_3, 32%), and sodium hydroxide (NaOH, 99%) were supplied by Merck. Sodium aluminate ($NaAlO_2$) was obtained from Nacalai, ethanol (absolute, analytical grade) from Fisher Scientific, Aerosil 300 fumed silica from Degussa, and toluene from J.T. Baker. The gases used for catalyst evaluation were of the purified grade (H_2, 99.9995%; N_2, 99.9995%; CO_2, 99.8%). All the chemicals were used without further purification.

2.2. Syntheses of MSS and MASS. In a typical synthesis, 150 mg of CTAB, 180 μL of TEOS, and 600 μL of toluene were dissolved in 24 mL of ethanol and stirred for 10 min. Meanwhile, 0−30 mg of $NaAlO_2$ and 0.75 mL of ammonia solution were dissolved in 26 mL of deionized water. The aqueous solution was then poured into the organic phase under stirring to form a clear mixture, which was aged at ambient temperature for 4 h. The precipitation was separated by centrifugation and washed with ethanol for 3 times before characterization. The products, macro-meso-microporous silica spheres and macro-meso-microporous aluminosilicate spheres, are named as MSS (without adding $NaAlO_2$) and MASS-*X*, respectively, where *X* stands for the amount (mg) of $NaAlO_2$ added. In some experiments the amount of water (w) or toluene (t) was varied, and the product is denoted as MASS-*X*w*Y* or MASS-*X*t*Y*, where *Y* stands for the amount of water (in mL) or the amount of toluene (in μL). The exact amounts of reagents used in each case are tabulated in SI-1 of the Supporting Information.

2.3. Drying and Calcination of Samples. The as-synthesized MSS and MASS were dried in an electrical oven at 60 °C overnight. Calcination was carried out at 500 °C for 4 h in static air. The products are referred to as MSS-cal and MASS-*X*cal, respectively.

2.4. Syntheses and Evaluation of Supported Cu/ZnO Catalysts. The MSS-cal and MASS-cal were wet-impregnated with dropwise addition of an aqueous solution of calculated amounts of $Cu(NO_3)_2 \cdot 3H_2O$, $Zn(NO_3)_2 \cdot 6H_2O$, and ethylenediamine where metal/EDA = 1/2 (mol/mol). After being kept at ambient temperature for 1 h, the paste was dried at 100 °C for 30 min and calcined at 350 °C for 2 h. The product is denoted as CZMSS or CZMASS-*X*. A 200 mg portion of such catalyst was diluted with 50 mg of Aerosil 300 SiO_2 and loaded into a tubular stainless steel reactor with a diameter of $^3/_8$ in. The catalyst was activated *in situ* with flowing 10% H_2/N_2 (50 std mL·min^{-1}) at 275 °C for 4 h and cooled to ambient temperature in the same gas mixture. The temperature was then increased to 250 °C with a gas mixture containing 72% of H_2, 24% of CO_2, and 4% of N_2 fed to the reactor at 60 std mL min^{-1}, and the pressure was increased to 20 bar by a backpressure regulator. After the reactor was stabilized for 1 h, composition of the effluent was monitored by gas chromatography for 20 h.

2.5. Characterization Methods. Morphological studies were carried out by transmission electron microscopy (TEM, JEM-2010, 200 kV), field-emission scanning electron microscopy (FESEM, JSM-6700F, 5 kV), and field-emission TEM (FETEM, JEM-2100F, 200 kV) capable of high-angle annular dark-field imaging (HAADF). Elemental composition was analyzed by energy dispersive X-ray spectroscopy (EDX, Oxford Instruments) coupled to scanning electron microscopy (SEM, JSM-5600LV, 15 kV). The presented composition of each sample is the average of at least 3 measurements at different sites. Elemental distribution of the catalysts was analyzed by EDX coupled to the FETEM operating in the HAADF mode. Crystallographic data was obtained by powder X-ray diffraction (XRD, Bruker D8 Advance, Cu Kα radiation at 1.5406 Å). More structural information was gathered by Fourier transformed infrared spectroscopy (FTIR, Bio-Rad FTS-3500ARX) and magic-angle spinning nuclear magnetic resonance (MAS NMR, Bruker DAX-400). The ^{27}Al NMR spectra were acquired at 104.3 MHz with a 5 μs pulse and 256 scans for dry powders contained in 4 mm rotors spinning at 8 kHz. Aqueous $Al(NO_3)_3$ was used as the reference for chemical shifts. N_2

DOI: 10.1021/acsami.5b03011
ACS Appl. Mater. Interfaces 2015, 7, 13578−13589

physisorption experiments were performed by a Quantachrome Instruments NOVA 4200e surface area and pore size analyzer at 77.3 K after samples were outgassed in flowing He at 200 °C for 3 h. Analysis of the effluent during catalyst evaluation was performed by gas chromatography (GC, Agilent 7890A with a thermal conductivity detector and a flame ionization detector).

3. RESULTS AND DISCUSSION

3.1. Effects of $NaAlO_2$. Typical morphologies of macro-meso-microporous silica spheres (MSS) and macro-meso-microporous aluminosilicate spheres (MASS) with different Al contents synthesized in the CTAB-stabilized oil-in-water microemulsion system are shown in Figure 1a−h. Overall, the products are uniform submicron spheres. As indicated in Figure 1i−l, the particle sizes exhibit unimodal distributions, and the small geometric standard deviations of ≤1.1 indicate low polydispersity of the MSS and MASS. Open channels in the macroporous range are observed in all of the spheres, which formed presumably around toluene droplets. The FESEM images (Figure 1b,d,f) show clearly that an increased amount of $NaAlO_2$ in the precursor solution resulted in a shrink in channel width and a denser distribution of channels. For MASS-30, however, only shallow indentations can be observed by FESEM (Figure 1h). With better clarity of internal structures through TEM, the indentations are confirmed to be discontinuous ellipsoidal voids that have openings to the surface (Figure 1g). Such aluminate-induced morphological changes have not been reported before, and we believe that they are a consequence of Hofmeister anion effects of $[Al(OH)_4]^-$ which will be discussed later in detail.

However, in the present system not only the concentration of $[Al(OH)_4]^-$, but also that of OH^-, increases with the addition of $NaAlO_2$. In Table 1, noticeable increase of the precursor solution pH is observed as $NaAlO_2$ is added, due to the partial hydrolysis of $[Al(OH)_4]^-$ (eq 2). Since OH^- is a cosmotropic ion, its effect has to be separated from that of $[Al(OH)_4]^-$ before attention is focused on the latter. A comparative study was therefore carried out where NaOH was used in place of $NaAlO_2$ to adjust the pH and all the other synthesis conditions were kept unchanged. As Figure 2a,b shows, the increase of pH did not cause morphological changes of the channels, which suggests negligible effect of OH^- in the present experimental conditions. Moreover, this experiment proves the role of Na^+ in the morphological control to be insignificant (comparable amounts of Na^+ were introduced by $NaAlO_2$ and NaOH). On the other hand, the change in pH does explain the size differences in MSS and MASS (Figure 1i−l). The increase followed by decrease of mean particle size with increasing pH matches reported observations in sol−gel synthesis of mesoporous silica, where the solubilization of silicate species and hence limited nucleation were cited as the reasons for larger particle size, and etching of silica as the cause of size reduction at a high pH range.[45,46]

It is demonstrated in Figure 1i−l that the considerable variation in Al content of the precursor solution did not affect the uniformity of particle size pronouncedly, while introducing Al during the sol−gel synthesis of silica particles has often been associated with ill-defined morphologies as mentioned in the Introduction. Comparing our synthetic method to those in most published works, we propose that the formation of microemulsion is the key factor in the successful morphological control. A microemulsion exhibits variable viscosity that usually increases with the volume fraction of the dispersed phase and

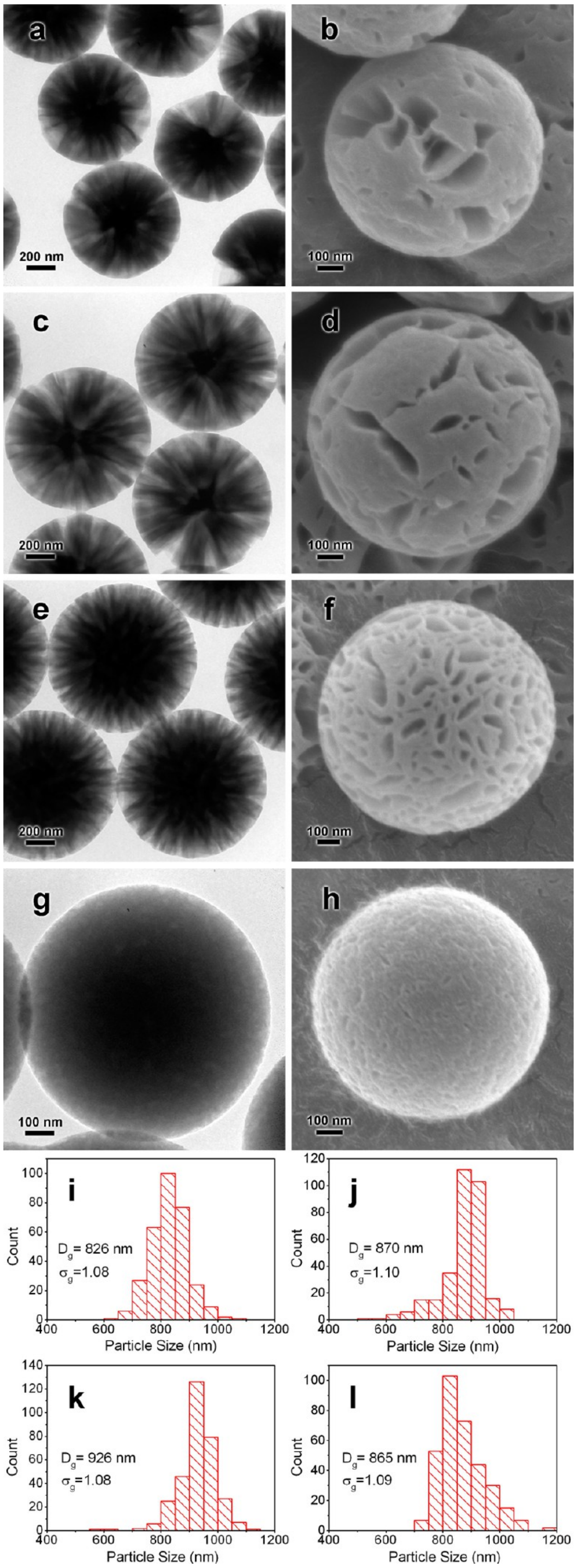

Figure 1. TEM, FESEM images, and particle size histograms of (a, b, i) MSS, (c, d, j) MASS-7.5, (e, f, k) MASS-15, and (g, h, l) MASS-30. The particle size distribution for each sample was determined by measuring at least 300 particles in TEM images: D_g, geometric mean diameter; σ_g, geometric standard deviation. TEM images of MASS-5, -10, -20, -25, -35, -40 samples are reported in the Supporting Information (SI-2).

Table 1. Solution pH and Elemental Composition of MSS and MASS with Different Amount of $NaAlO_2$ in Precursor

sample	precursor solution pH	product Al/Si	product Na/Al
MSS	11.34	0	n.a.
MASS-7.5	11.44	0.09	0.14
MASS-15	11.56	0.18	0.28
MASS-30	11.75	0.35	0.57

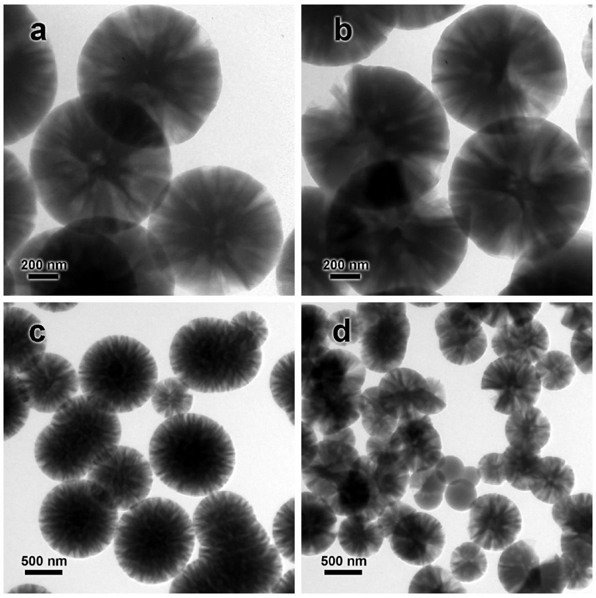

Figure 2. TEM images of (a, b) MSS synthesized with pH values adjusted to 11.57 and 11.81, respectively, using a NaOH solution, and (c, d) MASS-15 synthesized with continuous stirring for 6 and 10 min, respectively, after mixing of the organic phase and aqueous phase.

decrease with the droplet size of the dispersed phase.[47] Importantly, the apparent viscosity of the microemulsion can significantly exceed that of the pure phases forming it.[48] It is believed that the relatively higher viscosity impeded the Brownian motion of growing particles, preventing them from collision and aggregation. On the other hand, if mechanical energy is supplied to promote particle collision, the microemulsion establishment could also be disturbed, leading to less uniform products. To prove the role of collision in the particle growth, mechanical stirring was applied in the synthesis of MASS-15 to encourage turbulence and hence random motion of particles. Figure 2c,d show detrimental morphological effects of the stirring: the longer the stirring was applied, the lower the uniformity of formed products. As further evidence of the importance of forming microemulsion, MASS-30 has slightly higher numbers of large particles (Figure 1l) caused by particle aggregation. Considering the smaller volume of macrochannels in MASS-30 (Figure 1g,h) which indicates smaller volume of insoluble toluene droplets in the microemulsion, the aggregation of MASS-30 particles was very possibly due to relatively low viscosity of the precursor mixture.

Other than the morphological effects, direct consequences of the introduction of $NaAlO_2$ also include compositional changes of the product. In the synthesis of aluminosilicate functional materials, the ability to tightly control the Al content is crucial for obtaining desired acidity, which has a direct impact on the catalytic performance.[20,27] Table 1 shows that in the present system the Al content can be tuned facilely in a wide range of Al/Si = 0–0.35 (the macrochannels disappear if a larger amount of Al is introduced; see SI-2 of the Supporting Information); the Al/Si ratio in MASS is a simple linear function of the amount of $NaAlO_2$ in the precursor solution. Surprisingly, the Na/Al ratio also increases linearly as $NaAlO_2$ is added while in fact the amount of Na and Al introduced is always equal. To understand this phenomenon, another cationic species has to be considered, which in the present case is NH_4^+ originated from the hydrolysis of ammonia (eq 3). The ion exchange property of amorphous aluminosilicates has been well-documented.[49] This allows Na^+ and NH_4^+ to competitively adsorb onto the negatively charged MASS framework, and as a result, the relative amount of both adsorbed ions depends on their concentrations in the precursor solution (eq 4, where A stands for the MASS framework). On one hand, increasing the amount of $NaAlO_2$ raises the concentration of Na^+, and on the other hand, increasing the pH shifts the equilibrium in eq 3 toward the left. The combined effect is a larger Na^+/NH_4^+ ratio in solution which drives the equilibrium in eq 4 toward the adsorption of Na^+. In addition, CTA^+ may also partially balance the negative charge of MASS framework, but since the concentration of CTAB was maintained consistently, its role in the changing composition can be ignored.

$$NH_3{\cdot}H_2O \leftrightarrow NH_4^+ + OH^- \tag{3}$$

$$Na^+ + NH_4A \leftrightarrow NH_4^+ + NaA \tag{4}$$

The mesostructures of the as-synthesized MSS and MASS samples were characterized by powder XRD and high-resolution TEM. Figure 3 shows that the purely siliceous MSS sample possesses 2D hexagonal symmetry which is assigned to the *p6mm* plane group with a_0 = 2.77 nm. The peak assigned to the (20) plane is very broad and asymmetric, most probably due to presence of a partially overlapping (11) diffraction peak. With the addition of $NaAlO_2$, a coexisting mesophase appeared in MASS-7.5 and dominated in MASS-15. The new structure possesses cubic symmetry and is best assigned to the $Pm\bar{3}n$ space group with a_0 = 8.42 nm. The mesostructural transition is also reflected by increased pore size and altered pore arrangement directly observed by high-resolution TEM, as shown in SI-3 of the Supporting Information. However, a further increase in the amount of

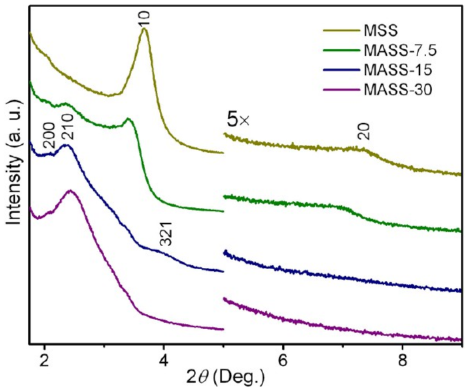

Figure 3. XRD patterns of as-synthesized MSS and MASS samples with different Al contents. Diffraction data above $2\theta = 5°$ is shown in 5× magnification. The curves have been shifted in the *y*-direction for better clarity.

$NaAlO_2$ did not change the symmetry, as indicated by the XRD pattern of MASS-30 (Figure 3). Mesostructural transition of siliceous materials due to Hofmeister anion effects has been reported in several works,[29,34,43] and a particularly relevant example[29] is the change from *p6mm* to $Pm\bar{3}n$ facilitated by the replacement of NO_3^-, a chaotropic anion, with cosmotropic SO_4^{2-}. In Scheme 1, comparison of the pore structures of the two mesophases shows higher curvature of pore walls and a more discrete pore network in $Pm\bar{3}n$, which reflects the dual effect of cosmotropic anions: smaller surfactant packing parameter and stronger intermicellar repulsion. The *p6mm*-to-$Pm\bar{3}n$ transition in the present system makes it reasonable to postulate a cosmotropic nature of $[Al(OH)_4]^-$.

Scheme 1. Mesostructural Tuning of MASS[a] Facilitated by the Hofmeister Anion Effect of $[Al(OH)_4]^-$

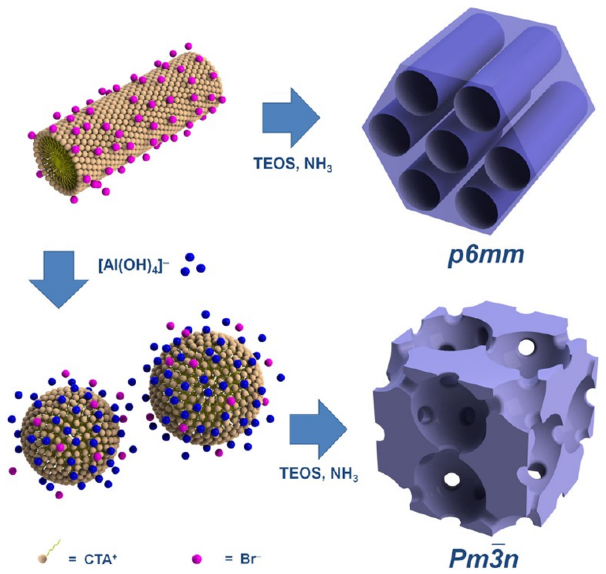

[a] The adsorption of $[Al(OH)_4]^-$ in replacement of Br^- on CTA^+ micelles increases the surface curvature, promoting the rod-to-sphere transformation. The difference in micelle shape is reflected in the mesostructures of the final MASS products.

The Hofmeister effects of $[Al(OH)_4]^-$ also explain the morphological change of the macrochannels. Scheme 2 illustrates that the toluene droplets in the present oil-in-water microemulsion are stabilized by CTA^+ ions and are thus positively charged. Similar to the smaller CTA^+ micelles more frequently encountered in the synthesis of mesoporous silica, they are expected to be subjected to Hofmeister effects. As the adsorption of more cosmotropic anions at the oil−water interface leads to higher stability and hence smaller sizes of the droplets,[41] the channels formed around the toluene droplets should also exhibit narrower widths, which has apparently occurred with the introduction of $NaAlO_2$ (Figure 1a−h). It is thus confirmed that $[Al(OH)_4]^-$, the dominant form of aluminate in solution, is cosmotropic in comparison to Br^- that originated from CTAB. Note that indeed $[Al(OH)_4]^-$ can bind easily to water molecules through hydrogen bonding.

Scheme 2. Shrinking of CTA^+-Stabilized Toluene Nanodroplets under the Hofmeister Anion Effect[a]

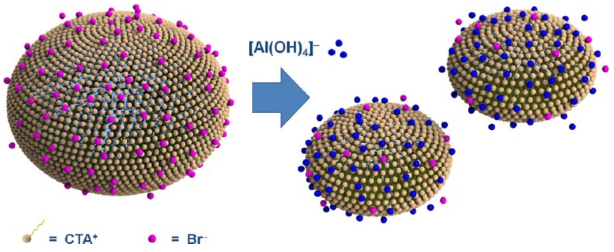

[a] The chaotropic bromide ion (Br^-) is replaced by cosmotropic $[Al(OH)_4]^-$. These nanodroplets (i.e., giant vesicles) are flexible enough to serve as soft templates for the formation of cone-shaped radial macrochannels in the MSS or MASS (TEM/FESEM images, Figure 1).

To reveal the textural properties of MSS and MASS, N_2 physisorption experiments were performed on calcined samples. As Figure 4a displays, they exhibit type I isotherms with narrow H4 hysteresis in general, suggesting the coexistence of micropores and mesopores.[50] In particular, the extension of hysteresis loops below the relative pressure of 0.2 is strong evidence of the presence of micropores, but the possibility of MSS and MASS being crystalline zeolites is ruled out by the absence of corresponding peaks in the XRD patterns (Figure 3). Moreover, the near-saturation adsorption at the relative pressure of $P/P_0 > 0.9$ provides useful information about the size and amount of macropores that correspond to the macrochannels observed by electron microscopy (Figure 1a−h). From MSS to MASS-15, the increasing slope of adsorption isotherms in the near-saturation range indicates an increasing amount of relatively small macropores ($d_{pore} = 50−100$ nm) which reflects the decrease in average channel width and/or increase in number of channels. However, as the channels continue to shrink and become discontinuous eventually in MASS-30, very few macropores are accessible to gas molecules, and a significant decrease in near-saturation adsorption is seen.

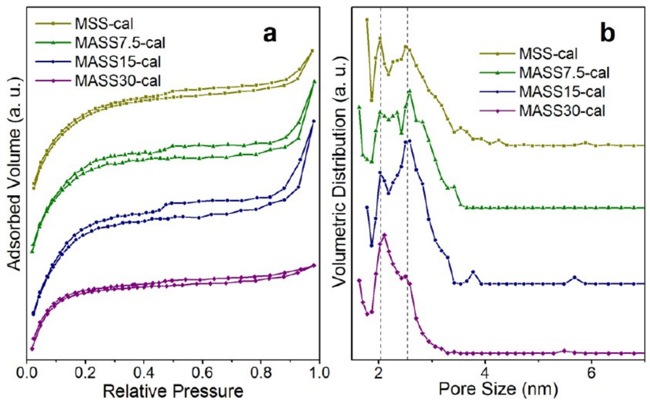

Figure 4. (a) N_2 physisorption isotherms and (b) differential volumetric pore size distribution of calcined MSS and MASS samples calculated by NLDFT. The curves have been shifted in the *y*-direction for better clarity. The dashed lines are a guide to the eye.

More precise details about the pore structure of calcined MSS and MASS samples can be obtained from the pore size distribution reported in Figure 4b. It should be pointed out that, in a $Pm\bar{3}n$ mesostructure, spherical pores are expected, the size of which cannot be determined with decent accuracy by the commonly used BJH method; instead, nonlocal density functional theory (NLDFT) calculations covering a wider range of adsorption modes are preferred.[35] Nonetheless, as a comparison, BJH pore analysis results are also reported in the

Supporting Information (SI-4). Here the NLDFT kernel of Quantachrome NovaWin was used assuming the adsorption of N_2 on silica with a cylindrical/spherical pore structure. The results in Figure 4b show clearly a bimodal size distribution of mesopores. As further evidence of the $Pm\bar{3}n$ structure, the bimodal distribution is consistent with published studies on the pore structure of $Pm\bar{3}n$ mesoporous silica.[51] Moreover, a comparison of micropore volume in Table 2 shows a decreasing trend as Al content increases, which matches the change in the XRD peak intensity of the *p6mm* mesophase (Figure 3). Considering in addition the relatively small size of pores that can be accommodated in the *p6mm* mesophase, the micropores are assigned to it while the mesopores in the size range 2−3 nm are attributed to the $Pm\bar{3}n$ mesophase. Note that although the micropore volumes of MASS-15cal and MASS-30cal are small compared with the samples containing less Al, they still contribute significantly to the total pore volume, which suggests the possibility of *p6mm* mesophase in both samples. In fact, the shoulder peaks observed in Figure 3 for MASS-15 and MASS-30 at $2\theta = 3.4°$ may be caused by its presence. Similarly, the notable amount of mesopores in MSS-cal could also mean that MSS contains $Pm\bar{3}n$ mesophase, but its diffraction signal might not be strong enough to generate well-resolved peaks. Overall the volume of mesopores increases with the Al content up to MASS-15 (Table 2), as also reflected by the height of hysteresis loops in Figure 4a. Such evolution is a result of the Hofmeister effect of $[Al(OH)_4]^-$; it causes the transformation of cylindrical micelles that form micropores in the *p6mm* mesophase into spherical micelles that are templates for mesopores in $Pm\bar{3}n$.[43] On the other hand, as depicted by Scheme 1 the narrow openings that connect the spherical pores in $Pm\bar{3}n$ could limit access of gas molecules and lead to "concealed" surfaces in the physisorption experiments. As a result, decreased surface area is observed with the progressive dominance of the $Pm\bar{3}n$ mesophase from MASS-7.5 to MASS-30 (Table 2). The dramatic drop in mesopore volume of MASS-30 can be attributed to the same effect. Interestingly, Figure 4b shows that the Al content does not affect the position of modes of the pore size distribution but only their relative height. The change in the relative population of larger and smaller mesopores is also reflected by the slight shift of XRD peaks of MASS-30 toward higher angles in Figure 3; it can be associated with the abundance of smaller mesopores which results in a smaller unit cell.

Table 2. Textural Properties of Calcined MSS/MASS with Different Amounts of $NaAlO_2$ in Precursor

sample	S_{BET} ($m^2\ g^{-1}$)	$V_{micro}{}^a$ ($cm^3\ g^{-1}$)	$V_{meso(2-30\ nm)}{}^a$ ($cm^3\ g^{-1}$)
MSS-cal	715	0.17	0.15
MASS-7.5cal	712	0.14	0.17
MASS-15cal	656	0.12	0.19
MASS-30cal	492	0.11	0.10

[a] Calculated with the NLDFT method.

Indeed, the hierarchical pore structures are confirmed by direct observation of the calcined samples through TEM. The images with lower magnification, i.e., Figure 5a,c,e,g, show that the spherical shape and macrochannels in all of the samples are stable to calcination at 500 °C; no scaling or channel collapsing are found. Under higher magnification (Figure 5b,d,f,h), micro- and mesopores are revealed. In MSS-cal and MASS-7.5cal particularly, pores aligned to the radial direction with openings 1.0−1.4 nm wide can be clearly seen. It becomes difficult to resolve the pore image as the Al content is further increased, most probably due to the spherical shape of pores in $Pm\bar{3}n$. For example, although extended pores can still be found by carefully observing the TEM image of MASS-15cal in Figure 5f, pores in MASS-30cal all appear as discrete low-contrast dots in Figure 5h.

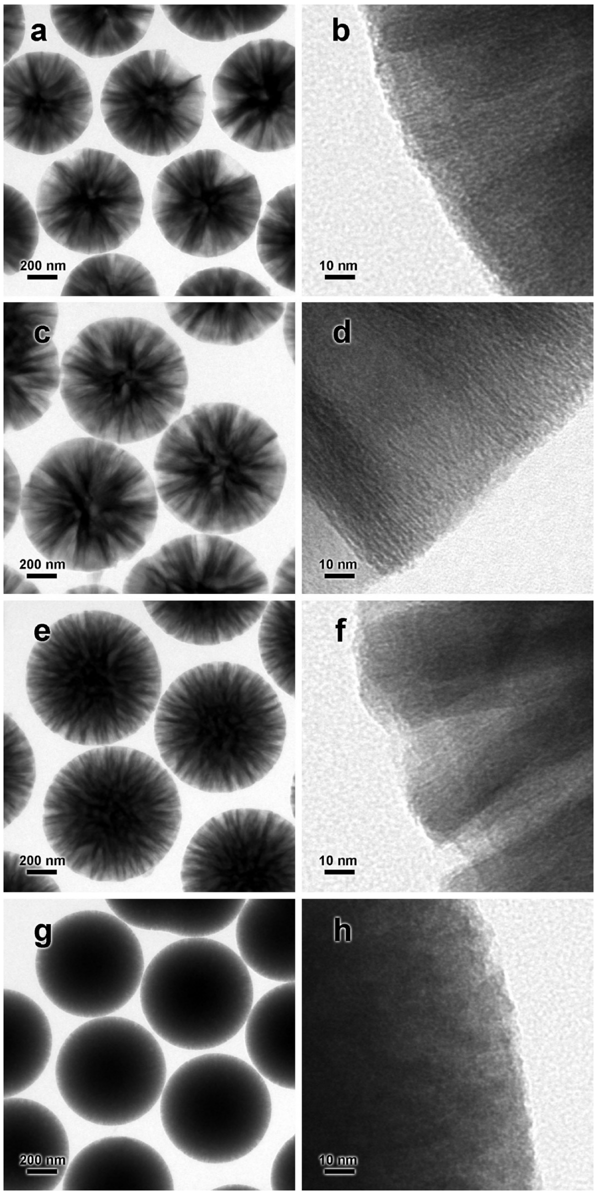

Figure 5. TEM images of calcined samples: (a, b) MSS-cal, (c, d) MASS-7.5cal, (e, f) MASS-15cal, and (g, h) MASS-30cal.

Atomic-scale structures of MSS and MASS were studied by NMR and FTIR techniques. The ^{27}Al magical-angle spinning NMR spectra in Figure 6 show only one type of Al in the as-synthesized MASS, whose signal strength increases with the Al content. The peak is located at around 54.5 ppm regardless of the Al content, indicating that 100% of the Al is tetrahedrally coordinated.[30] The incorporation of Al into the tetrahedral centers of the aluminosilicate framework is desirable in the synthesis of acidic catalyst supports, as the Al−OH−Si bridge thus formed provides stronger acid sites that are more active than those created by octahedral Al.[52] Compared with aluminosilicates synthesized in acidic and/or hydrothermal

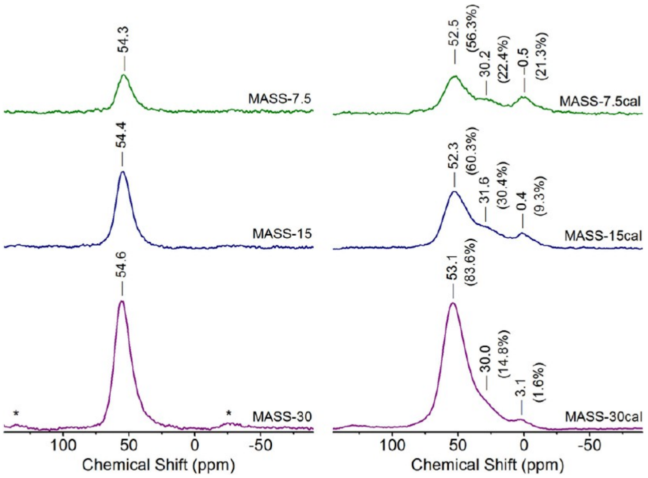

Figure 6. ^{27}Al magical-angle spinning NMR spectra of MASS samples before/after calcination. Numbers in parentheses are percentages of deconvoluted individual peak areas among total peak areas. Spinning sidebands are marked by asterisks.

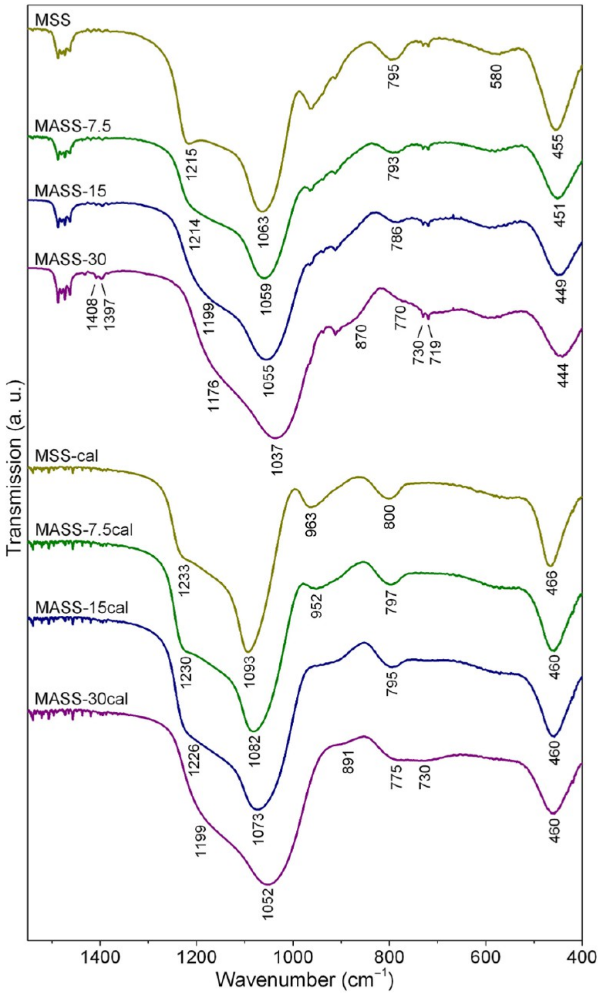

Figure 7. FTIR spectra of as-synthesized and calcined MSS and MASS samples.

conditions,[18,19,24,28] the higher percentage of tetrahedrally coordinated Al is probably a result of the chemical state of Al in the precursor solution. In neutral-to-acidic solutions, the principal forms of Al^{3+} are octahedral $[Al(H_2O)_6]^{3+}$ and its hydrolyzed hydroxy analogues. During the synthesis of aluminosilicates, the hydrolysis and condensation of octahedral Al^{3+} complexes compete with the incorporation of Al, usually resulting in noticeable formation of extra-framework Al species that appear as a peak at ca. 0 ppm in ^{27}Al magical-angle spinning NMR spectra.[30] In contrast, the present system was kept at a relatively high alkalinity, and Al was introduced as a stable tetrahedral complex $[Al(OH)_4]^-$, which prevented the competing reactions during the mild sol−gel process. However, after calcination, 5-coordinated Al (peaks at ca. 30 ppm in NMR spectra) and octahedral Al species appear (Figure 6),[30] though the majority of Al still remains in tetrahedral centers, particularly in MASS-30cal sample.

The effect of Al incorporation is also reflected by FTIR spectroscopy. In Figure 7, typical mid-IR absorption bands of amorphous silica are observed for all of the as-synthesized and calcined samples. For as-synthesized MSS, the strong band at 1063 cm^{-1} with a shoulder at 1215 cm^{-1} and the band at 795 cm^{-1} can be assigned to the asymmetric and symmetric stretching of Si−O in SiO_4 tetrahedra, respectively.[53] Another strong band at 455 cm^{-1} is due to vibration of interconnected SiO_4 tetrahedra.[54] A weak band near 580 cm^{-1} is attributed to the bending mode of surface silanol group Si−OH,[55] though its overlap with vibration modes of Si−O−Si ring structures is possible.[23] The surface silanol group should also exhibit a stretching mode at around 960 cm^{-1},[56] but in this case the latter cannot be resolved due to heavy overlap with absorption bands of CTAB. As the Al content increases in the as-synthesized samples, a red-shift is observed in all of the Si−O vibration modes, which has been attributed to the incorporation of Al in silica frameworks.[54,57] It is believed that the lower electronegativity of Al compared with Si causes the immediately neighboring O to gain extra electron density, thus weakening the Si−O bond. Notably, a new band at 870 cm^{-1} emerges in the spectrum of MASS-30 that is assigned to the interactive vibration of AlO_4 tetrahedra.[58] It is apparently a result of extensive incorporation of Al that increases the probability of neighboring Al coordination centers. In addition, two bands at 1408 and 1397 cm^{-1} assigned to adsorbed NH_4^+ are also observed for MASS-30,[59−61] further confirming the competitive adsorption of NH_4^+ and Na^+ during the sol−gel synthesis (eq 4). It is worth pointing out that NH_4^+ usually appears as a single peak at 1400 cm^{-1}, but in the present case the overlap with OH bending modes of hydrogen-bonded H_2O manifested the peak as a doublet.

After calcination, a noticeable blue-shift occurred in all of the absorption bands related to the vibration modes of Si−O which indicates a denser framework in general. Moreover, the red-shifts caused by Al incorporation persisted; the Al still remained in the framework. As a result of thermally induced condensation of surface silanol groups, the intensity of the broad bands near 580 cm^{-1} decreased. On the other hand, the complete removal of CTAB during calcination allowed for the stretching mode of Si−OH to be resolved. For MSS-cal it is located at 963 cm^{-1}. Similar to the stretching modes of framework Si−O, it also experiences a red-shift due to incorporation of Al, and meanwhile, a decreasing trend in its intensity is observed. The red-shift can be explained by the presence of less electronegative Al neighboring the silanol, and the decreasing band intensity suggests that Al promotes the condensation of silanol groups, probably by forming Si−O−Al linkages.[62] Accompanying the attenuation of Si−OH vibration modes, two bands at 891 and 730 cm^{-1} emerged gradually which are assigned to the vibration modes of interconnected and isolated AlO_4 tetrahedra, respectively.[58,63] It should be pointed out that the absorption band of isolated AlO_4 is also present in the spectrum of as-synthesized MASS-30, but it is covered by the absorption bands of CTAB at 719 and 730 cm^{-1}.

3.2. Effects of Water. Figure 8a−c presents the morphology of MASS-15 synthesized with varied amounts of water. The most obvious morphological effect of water is inhibition of particle aggregation, which can be partially understood as a result of a change in the relative rate of TEOS hydrolysis and silicate condensation. As shown in eqs 5 and 6, the sol−gel synthesis of siliceous materials can be considered a reaction series: TEOS is first hydrolyzed into less ethylated species which (represented by H_4SiO_4 here for clear presentation) then undergo condensation to form oligomers and eventually SiO_2 precipitate. The increase in water concentration speeds up the hydrolysis and hence the formation of poorly soluble condensed silicates. From the classic view of crystal growth,[64] the large degree of supersaturation favors burst nucleation. If followed by a controlled growth step, narrow particle size distribution can be obtained. In the present system it could be achieved by depletion of Si source before secondary nucleation occurred and/or particles coalesced due to Brownian motion-induced collision. The use of more than 25 mL of water has apparently created such optimal conditions (Figures 8b,c and 1e). In addition, reaction between surface silanol groups and silica sources has been proposed to be important in the growth stage of mesoporous silica spheres,[65] which can be viewed as a heterogeneous condensation step (eq 7). As shown in eq 8, condensation between silanol groups is also possible, causing particle coalescence upon collision. The addition of water may stabilize the silanol group and prevent the formation of interparticle linkages (eq 8), hence contributing to a better size uniformity. On the other hand, the addition of water could also drive a larger amount of toluene into the dispersed phase in the microemulsion and hence result in higher viscosity, which in turn slows down particle coalescence.

$$Si(OC_2H_5)_4 + xH_2O \rightarrow Si(OC_2H_5)_{4-x}(OH)_x + xC_2H_5OH \quad (5)$$

$$nH_4SiO_4 \rightarrow nSiO_2 + 2nH_2O \quad (6)$$

$$Si{-}OH + H_4SiO_4 \rightarrow Si{-}O{-}Si(OH)_3 + H_2O \quad (7)$$

$$Si{-}OH + HO{-}Si \rightarrow Si{-}O{-}Si + H_2O \quad (8)$$

In a comparison of the N_2 sorption isotherms of MASS-15 synthesized with increasing amounts of water (Figure 9a), slightly enhanced near-saturation adsorption can be observed which indicates an increase in macropore volume. Corresponding morphological evidence can also be obtained by careful comparison among parts a−c of Figure 8. Such an increase reflects the volume change of toluene nanodroplets due to lower solubility of toluene in a water-rich mixture. Moreover, a closer look at the textural properties of these samples in Table 3 shows that the surface area and mesopore volume are sensitive to the water content; they decrease to similar extends as the amount of water increases. The decrease can be attributed to the lower structural orderliness as a result of fast particle growth.[66] In contrast, the mesopore size distribution (Figure 9b) and micropore volume (Table 3) are not affected by the amount of water.

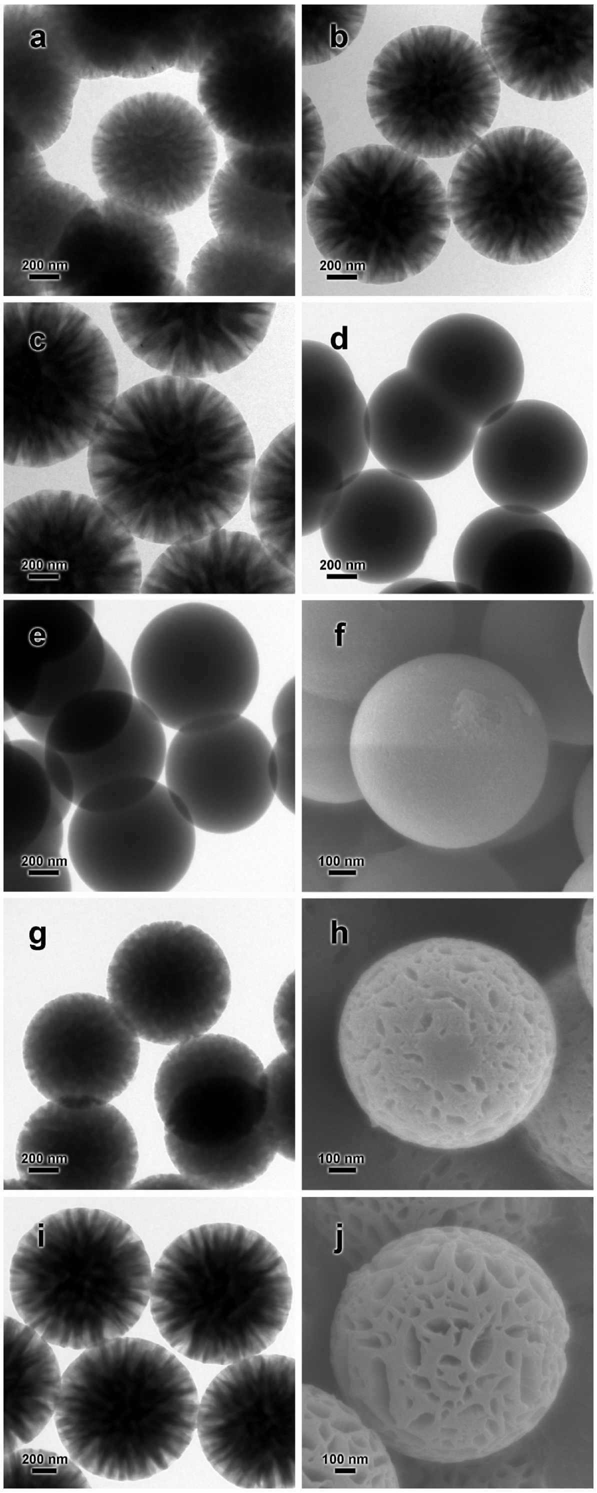

Figure 8. TEM and FESEM images of as-synthesized (a) MASS-15w24, (b) MASS-15w25, (c) MASS-15w27, (d) MASS-15t0, (e, f) MASS-15t100, (g, h) MASS-15t300, and (i, j) MASS-15t750. Images of MASS synthesized with other amounts of water are reported in the Supporting Information (SI-5).

3.3. Effects of Toluene. As the structure-directing agent of macropores, toluene significantly affects their formation in the present system. The electron microscope images in Figure 8d−f show that no macropores are formed without or with 100 μL of

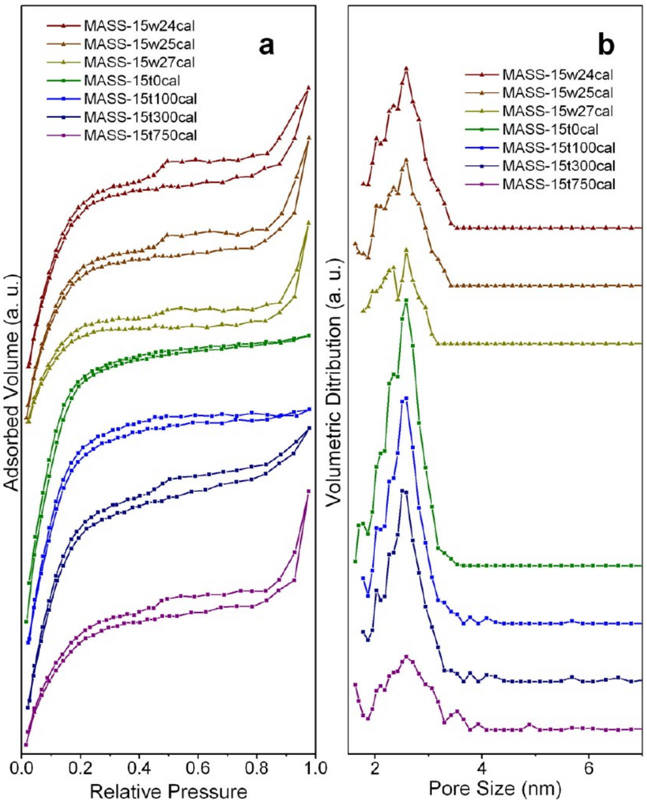

Figure 9. (a) N_2 adsorption−desorption isotherms and (b) volumetric pore size distribution of calcined MASS-15 synthesized with different amounts of toluene and water. The curves have been shifted in the *y*-direction for better clarity.

Table 3. Textural Properties of Calcined MASS-15 with Different Amount of Water and Toluene in Precursor

sample	S_{BET} (m^2 g^{-1})	V_{micro}^{a} (cm^3 g^{-1})	$V_{meso(2-30\ nm)}$^{a} (cm^3 g^{-1})
MASS-15w24cal	797	0.10	0.27
MASS-15w25cal	694	0.11	0.22
MASS-15w27cal	545	0.11	0.14
MASS-15t0cal	856	0.05	0.35
MASS-15t100cal	858	0.08	0.31
MASS-15t300cal	830	0.09	0.31
MASS-15t750cal	523	0.09	0.17

^{a}Calculated with the NLDFT method.

toluene added. In these cases the concentration of toluene is below the solubility limit, and instead of microemulsion a homogeneous precursor solution is formed. Particle aggregation can be observed, probably due to the lower viscosity of the homogeneous solution which could not dampen the collision between forming particles effectively. When the amount of toluene is further increased to 300 and 750 μL, macropores emerge and grow in volume, and the uniformity of particle size is improved (Figure 8g−j). The changes in macropore volume are also reflected by N_2 sorption isotherms plotted in Figure 9a; the near-saturation adsorption is negligible for MASS-15t0cal and MASS-15t100cal, while it becomes significant for products synthesized with larger amounts of toluene. Additional effects of introducing toluene are reflected by a summary of textural properties in Table 3. It is clear that the surface area decreases significantly only when more than 300 μL of toluene is added, and the mesopore volume also follows a similar trend. Considering the trend in the evolution of macropores, this phenomenon should be associated with the presence of microemulsion. We believe that the formation of microemulsion consumes CTA^+ as stabilizing agent at the oil−water interface and decreases the amount of CTA^+ available to form mesopore-directing micelles. Consequently, the mesopore volume (Table 3) as well as the closely related surface area decreases. Since an increase in the amount of water can lead to larger volume of toluene nanodroplets, the same mechanism should also play a role in the dependence of surface area and pore volume on water content discussed earlier. In addition, the presence of toluene seems to promote the formation of micropores, but its amount is less important. The pore size distribution in Figure 9b does not indicate any shift of modal sizes, and the swelling of micelles can be excluded. It is thus speculated that the dissolved toluene enhances interaction between CTA molecules and leads to an increased number of cylindrical micelles that form micropores.

3.4. Effects of Other Synthesis Parameters. In addition to the amount of water and toluene, other synthesis parameters including the amounts of NH_3, CTAB, and TEOS were also studied. The results are reported in the Supporting Information (SI-6). Basically, they exhibit less significant morphological effects.

3.5. Catalytic Experiments. Porous silica has a long history of being used as catalyst supports. In recent years as global warming has gained public awareness, interest in the catalytic conversion of CO_2, the major greenhouse gas, has dramatically increased.[67] The majority of works under this topic have been focused on Cu-based catalysts which were traditionally used for methanol synthesis. In this context we illustrate the application of the present MSS and MASS-15 by loading them with a Cu/ZnO composite (the resultant catalysts are denoted as CZMSS and CZMASS-15, respectively) and testing the catalysts in the model reaction of CO_2 hydrogenation. A nominal metal loading of 5% Cu and 3% ZnO by weight was used. CO, methanol, and dimethyl ether (DME) were detected to be the only carbon-containing products. Additionally, catalytic properties of more complex catalysts based on MSS/MASS (e.g., Cu/ZnO-loaded MASS with its Na content exchanged with Mg and Cu/ZnO/Ga_2O_3-loaded MASS) were also investigated, and the results are presented in the Supporting Information (SI-7).

Figure 10a shows that, without incorporation of Al, the CZMSS exhibits high specific activity comparable to published results of fumed SiO_2-loaded Cu/ZnO catalysts (ca. 56 mol CO_2 kg^{-1} metal h^{-1} at steady state).[68] Slow increase in the activity and organic selectivity can be observed in Figure 10a,b, respectively, which indicates continuous surface reconstruction of the active component promoting the formation of methanol. It has been suggested that Zn-doped atom "steps" on Cu surface, having much higher methanol synthesis activity than their counterparts on pure Cu surface, are the active sites in industrial Cu/ZnO/Al_2O_3 catalysts,[69] and the aforementioned surface reconstruction can be regarded as diffusion of Zn toward Cu surfaces. However, Figure 10c shows that without functionalization of the silica support, no DME formed using the Al-free CZMSS catalyst.

As a result of Al incorporation, remarkable change in activity and product composition can be observed in Figure 10a,c. For example, CZMASS-15 catalyst shows a lower specific activity but a significant increase in DME product, which reflects the acidity of MASS-15. It has been generally accepted that, in

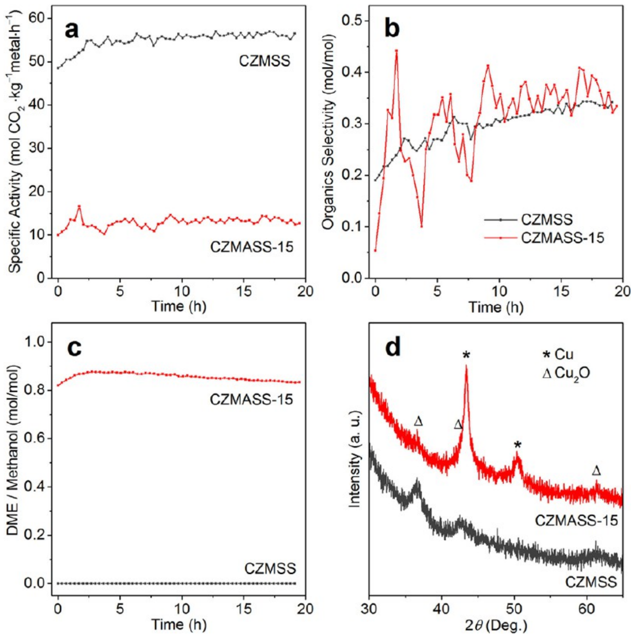

Figure 10. Results from catalyst evaluation of CZMSS and CZMASS-15: (a) specific activity (CO_2 consumption rate normalized by total amount of Cu and Zn in catalyst), (b) organic selectivity (rate of CO_2 converting to dimethyl ether and methanol divided by the total CO_2 consumption rate), (c) mole ratio between dimethyl ether and methanol in product stream, and (d) XRD patterns of spent catalysts.

methanol synthesis, DME is formed at Brønsted acid sites by the dehydration of methanol.[67] The CZMASS-15 can thus be viewed as a bifunctional catalyst where the Cu/ZnO composite catalyzes methanol synthesis and the aluminosilicate support acts as solid acid catalyzing methanol dehydration. Assuming that DME was only derived from methanol as the intermediate, the conversion of methanol to DME reached 61%. Although the calculated organic selectivity for CZMASS-15 fluctuates greatly in Figure 10b due to random error being magnified by the low conversion, the overall trend follows that of CZMSS. Surface reconstruction similar to that in CZMSS can be expected.

After the catalytic reaction, the spent catalysts were analyzed by XRD. Figure 10d shows that Cu and/or Cu_2O was present in the samples. Considering the strongly reducing environment of the reaction, Cu_2O should not exist in significant amounts during the reaction; it was formed presumably by the oxidation of Cu in air. Despite large efforts in controlling the exposure of the samples to air, their oxidation which continued in the sample chamber of the diffractometer was inevitable. Nevertheless, the degree of oxidation and status of the remaining unoxidized Cu particles provide valuable insights about the catalyst. CZMSS exhibits particularly weak diffraction peaks of Cu, and the oxidation of Cu particles was practically complete. It suggests a highly dispersed status and very reactive surfaces of Cu, which explain the higher activity of CZMSS (Figure 10a). In contrast, CZMASS-15 shows a strong diffraction signal from Cu, which is an indication of more severe sintering than CZMSS. In addition, Cu_2O formation is insignificant for CZMASS-15 probably due to limited Cu surface area. The main factor in the Cu sintering of CZMASS-15 is believed to be limited pore accessibility during impregnation. As discussed earlier, the $Pm\overline{3}n$ mesophase in MASS-15 consists of spherical pores connected by narrow holes where considerable surface tension may prevent solutions from wetting the entire pore network. Compared with the case of MSS where the cylindrical pores of the *p6mm* mesophase are more accessible, a larger portion of metal precursors might be kept near the surface of MASS-15. During calcination and catalyst activation, the metal precursors on the surface sinter more easily to reduce dispersity of the metal particles and hence activity. For CZMSS, it is possible that the metal particles formed deep inside MSS were confined by the pore walls, which prevented sintering.[70]

4. CONCLUSIONS

We have demonstrated for the first time the single-step synthesis of monodisperse aluminosilicate spheres with hierarchical macro-meso-microporous structure at room temperature. The CTAB-stabilized microemulsion system provided multiscale soft templates for the hierarchical pore structure where micropores contributed up to over 50% of total pore volume. Meanwhile, the formation of microemulsion was shown to be the key to obtaining monodisperse particles, most probably due to its rheological properties. In addition, the alkaline environment of the precursor mixture allowed for stable existence of $[Al(OH)_4]^-$ and hence incorporation of Al in an exclusively four-coordinated state with an Al/Si ratio conveniently tunable between 0 and 0.35. The present work has illustrated the generality and practicality of Hofmeister anion effects in materials synthesis, linking two important topics about siliceous materials, namely, chemical functionalization and pore engineering. To the best of our knowledge, simultaneous tuning of macro-, meso-, and micropores with the incorporation of heteroatom in silica and, in particular, synthesis of monodisperse aluminosilicate particles with such hierarchical structures have not been reported before. The possibility of achieving monodispersity of product particles will also facilitate our future development and utilization of this class of novel porous materials.

■ ASSOCIATED CONTENT

Ⓢ Supporting Information

Tabulation of synthesis parameters of MSS/MASS samples, TEM images of MASS synthesized under various conditions, and more characterization and CO_2 hydrogenation results of the supported catalysts. The Supporting Information is available free of charge on the ACS Publications website at DOI: 10.1021/acsami.5b03011.

■ AUTHOR INFORMATION

Corresponding Author

*E-mail: chezhc@nus.edu.sg.

Notes

The authors declare no competing financial interest.

■ ACKNOWLEDGMENTS

Y.S. would like to thank National University of Singapore (NUS) for providing his postgraduate scholarship. The authors gratefully acknowledge the financial support provided by the Ministry of Education, Singapore, NUS, and GSK Singapore. This project is also partially funded by the National Research Foundation (NRF), Prime Minister's Office, Singapore, under its Campus for Research Excellence and Technological Enterprise (CREATE) program.

REFERENCES

(1) Kresge, C. T.; Leonowicz, M. E.; Roth, W. J.; Vartuli, J. C.; Beck, J. S. Ordered Mesoporous Molecular Sieves Synthesized by a Liquid-Crystal Template Mechanism. *Nature* **1992**, *359*, 710−712.

(2) Davis, M. E. Ordered Porous Materials for Emerging Applications. *Nature* **2002**, *417*, 813−821.

(3) Thoelen, C.; Van de Walle, K.; Vankelecom, I. F. J.; Jacobs, P. A. The Use of M41S Materials in Chiral HPLC. *Chem. Commun. (Cambridge, U.K.)* **1999**, 1841−1842.

(4) Du, X.; Shi, B.; Liang, J.; Bi, J.; Dai, S.; Qiao, S. Z. Developing Functionalized Dendrimer-Like Silica Nanoparticles with Hierarchical Pores as Advanced Delivery Nanocarriers. *Adv. Mater.* **2013**, *25*, 5981−5985.

(5) Dou, J.; Zeng, H. C. Targeted Synthesis of Silicomolybdic Acid (Keggin Acid) Inside Mesoporous Silica Hollow Spheres for Friedel-Crafts Alkylation. *J. Am. Chem. Soc.* **2012**, *134*, 16235−16246.

(6) Zeng, H. C. Integrated Nanocatalysts. *Acc. Chem. Res.* **2013**, *46*, 226−235.

(7) Liu, Y.; Pinnavaia, T. J. Aluminosilicate Nanoparticles for Catalytic Hydrocarbon Cracking. *J. Am. Chem. Soc.* **2003**, *125*, 2376−2377.

(8) Schacht, S.; Huo, Q.; Voigt-Martin, I. G.; Stucky, G. D.; Schüth, F. Oil-Water Interface Templating of Mesoporous Macroscale Structures. *Science* **1996**, *273*, 768−771.

(9) Polshettiwar, V.; Cha, D.; Zhang, X.; Basset, J. M. High-Surface-Area Silica Nanospheres (KCC-1) with a Fibrous Morphology. *Angew. Chem., Int. Ed.* **2010**, *49*, 9652−9656.

(10) Moon, D.-S.; Lee, J.-K. Tunable Synthesis of Hierarchical Mesoporous Silica Nanoparticles with Radial Wrinkle Structure. *Langmuir* **2012**, *28*, 12341−12347.

(11) Hwang, J.; Jo, C.; Hur, K.; Lim, J.; Kim, S.; Lee, J. Direct Access to Hierarchically Porous Inorganic Oxide Materials with Three-Dimensionally Interconnected Networks. *J. Am. Chem. Soc.* **2014**, *136*, 16066−16072.

(12) Petkovich, N. D.; Stein, A. Controlling Macro- and Mesostructures with Hierarchical Porosity through Combined Hard and Soft Templating. *Chem. Soc. Rev.* **2013**, *42*, 3721−3739.

(13) Wang, D. P.; Zeng, H. C. Creation of Interior Space, Architecture of Shell Structure, and Encapsulation of Functional Materials for Mesoporous SiO_2 Spheres. *Chem. Mater.* **2011**, *23*, 4886−4899.

(14) Corma, A. From Microporous to Mesoporous Molecular Sieve Materials and Their Use in Catalysis. *Chem. Rev.* **1997**, *97*, 2373−2419.

(15) Li, Z.; Zeng, H. C. Armored MOFs: Enforcing Soft Microporous MOF Nanocrystals with Hard Mesoporous Silica. *J. Am. Chem. Soc.* **2014**, *136*, 5631−5639.

(16) Fan, W.; Snyder, M. A.; Kumar, S.; Lee, P.-S.; Yoo, W. C.; McCormick, A. V.; Lee Penn, R.; Stein, A.; Tsapatsis, M. Hierarchical Nanofabrication of Microporous Crystals with Ordered Mesoporosity. *Nat. Mater.* **2008**, *7*, 984−991.

(17) Schumacher, K.; du Fresne von Hohenesche, C.; Unger, K. K.; Ulrich, R.; Du Chesne, A.; Wiesner, U.; Spiess, H. W. The Synthesis of Spherical Mesoporous Molecular Sieves MCM-48 with Heteroatoms Incorporated into the Silica Framework. *Adv. Mater.* **1999**, *11*, 1194−1198.

(18) Vinu, A.; Murugesan, V.; Böhlmann, W.; Hartmann, M. An Optimized Procedure for the Synthesis of AlSBA-15 with Large Pore Diameter and High Aluminum Content. *J. Phys. Chem. B* **2004**, *108*, 11496−11505.

(19) Ribeiro Carrott, M. M. L.; Conceição, F. L.; Lopes, J. M.; Carrott, P. J. M.; Bernardes, C.; Rocha, J.; Ramôa Ribeiro, F. Comparative Study of Al-MCM Materials Prepared at Room Temperature with Different Aluminium Sources and by some Hydrothermal Methods. *Microporous Mesoporous Mater.* **2006**, *92*, 270−285.

(20) Muthu Kumaran, G.; Garg, S.; Soni, K.; Kumar, M.; Gupta, J. K.; Sharma, L. D.; Rama Rao, K. S.; Murali Dhar, G. Synthesis and Characterization of Acidic Properties of Al-SBA-15 Materials with Varying Si/Al Ratios. *Microporous Mesoporous Mater.* **2008**, *114*, 103−109.

(21) Russo, P. A.; Ribeiro Carrott, M. M. L.; Carrott, P. J. M.; Lopes, J. M.; Ramôa Ribeiro, F.; Rocha, J. Structure and Catalytic Activity of Al-MCM-48 Materials Synthesised at Room Temperature: Influence of the Aluminium Source and Calcination Conditions. *Microporous Mesoporous Mater.* **2008**, *114*, 293−302.

(22) Lemaire, A.; Su, B.-L. Tailoring the Porous Hierarchy and the Tetrahedral Aluminum Content by using Carboxylate Ligands: Hierarchically Structured Macro-Mesoporous Aluminosilicates from a Single Molecular Source. *Langmuir* **2010**, *26*, 17603−17616.

(23) Wang, L.; Wang, A.; Li, X.; Zhou, F.; Hu, Y. Highly Acidic Mesoporous Aluminosilicates Prepared from Preformed HY Zeolite in Na_2SiO_3 Alkaline Buffer System. *J. Mater. Chem.* **2010**, *20*, 2232−2239.

(24) El-Safty, S.; Shahat, A.; Ogawa, K.; Hanaoka, T. Highly Ordered, Thermally/Hydrothermally Stable Cubic Ia3d Aluminosilica Monoliths with Low Silica in Frameworks. *Microporous Mesoporous Mater.* **2011**, *138*, 51−62.

(25) Lemaire, A.; Wang, Q.-Y.; Wei, Y.; Liu, Z.; Su, B.-L. Hierarchically Structured Meso-Macroporous Aluminosilicates with High Tetrahedral Aluminium Content in Acid Catalysed Esterification of Fatty Acids. *J. Colloid Interface Sci.* **2011**, *363*, 511−520.

(26) El-Safty, S. A.; Shenashen, M. A.; Ismael, M.; Khairy, M. Mesocylindrical Aluminosilica Monolith Biocaptors for Size-Selective Macromolecule Cargos. *Adv. Funct. Mater.* **2012**, *22*, 3013−3021.

(27) Zou, J.-J.; Chang, N.; Zhang, X.; Wang, L. Isomerization and Dimerization of Pinene using Al-Incorporated MCM-41 Mesoporous Materials. *ChemCatChem* **2012**, *4*, 1289−1297.

(28) Choi, Y.; Yun, Y. S.; Park, H.; Park, D. S.; Yun, D.; Yi, J. A Facile Approach for the Preparation of Tunable Acid Nano-Catalysts with a Hierarchically Mesoporous Structure. *Chem. Commun. (Cambridge, U.K.)* **2014**, *50*, 7652−7655.

(29) Fu, W. H.; Wu, S. J.; Wang, Y. M.; He, M. Y. Cubic *Pm3n* Supermicroporous Silicas and Aluminosilicates Templated by Short-Chain Alkyltrimethylammonium Surfactants. *J. Mater. Chem. A* **2014**, *2*, 14908−14917.

(30) Parker, W. O.; Wegner, S. Aluminum in Mesoporous Silica−Alumina. *Microporous Mesoporous Mater.* **2012**, *158*, 235−240.

(31) Radnai, T. Structure of Aqueous Sodium Aluminate Solutions: A Solution X-ray Diffraction Study. *J. Phys. Chem. A* **1998**, *102*, 7841−7850.

(32) Sipos, P. The Structure of Al(III) in Strongly Alkaline Aluminate Solutions—A Review. *J. Mol. Liq.* **2009**, *146*, 1−14.

(33) Wu, S.-H.; Mou, C.-Y.; Lin, H.-P. Synthesis of Mesoporous Silica Nanoparticles. *Chem. Soc. Rev.* **2013**, *42*, 3862−3875.

(34) Che, S.; Li, H.; Lim, S.; Sakamoto, Y.; Terasaki, O.; Tatsumi, T. Synthesis Mechanism of Cationic Surfactant Templating Mesoporous Silica under an Acidic Synthesis Process. *Chem. Mater.* **2005**, *17*, 4103−4113.

(35) Wan, Y.; Zhao, D. On the Controllable Soft-Templating Approach to Mesoporous Silicates. *Chem. Rev.* **2007**, *107*, 2821−2860.

(36) Hofmeister, F. Zur Lehre von der Wirkung der Salze. *Arch. Exp. Pathol. Pharmakol.* **1888**, *24*, 247−260.

(37) Leontidis, E. Hofmeister Anion Effects on Surfactant Self-Assembly and the Formation of Mesoporous Solids. *Curr. Opin. Colloid Interface Sci.* **2002**, *7*, 81−91.

(38) Jakubowska, A. Interactions of Different Counterions with Cationic and Anionic Surfactants. *J. Colloid Interface Sci.* **2010**, *346*, 398−404.

(39) Subramanian, V.; Ducker, W. A. Counterion Effects on Adsorbed Micellar Shape: Experimental Study of the Role of Polarizability and Charge. *Langmuir* **2000**, *16*, 4447−4454.

(40) Zhao, D.; Huo, Q.; Feng, J.; Chmelka, B. F.; Stucky, G. D. Nonionic Triblock and Star Diblock Copolymer and Oligomeric Surfactant Syntheses of Highly Ordered, Hydrothermally Stable, Mesoporous Silica Structures. *J. Am. Chem. Soc.* **1998**, *120*, 6024−6036.

(41) Murgia, S.; Monduzzi, M.; Ninham, B. W. Hofmeister Effects in Cationic Microemulsions. *Curr. Opin. Colloid Interface Sci.* **2004**, *9*, 102−106.

(42) Wojciechowski, K.; Bitner, A.; Warszyński, P.; Żubrowska, M. The Hofmeister Effect in Zeta Potentials of CTAB-Stabilised Toluene-in-Water Emulsions. *Colloids Surf., A* **2011**, *376*, 122−126.

(43) Liu, M.-C.; Sheu, H.-S.; Cheng, S. Anion-Exchange Induced Phase Transformation of Mesostructured Silica. *J. Am. Chem. Soc.* **2009**, *131*, 3998−4005.

(44) Zhou, Y.; Zeng, H. C. Simultaneous Synthesis and Assembly of Noble Metal Nanoclusters with Variable Micellar Templates. *J. Am. Chem. Soc.* **2014**, *136*, 13805−13817.

(45) Lu, F.; Wu, S.-H.; Hung, Y.; Mou, C.-Y. Size Effect on Cell Uptake in Well-Suspended, Uniform Mesoporous Silica Nanoparticles. *Small* **2009**, *5*, 1408−1413.

(46) Chiang, Y.-D.; Lian, H.-Y.; Leo, S.-Y.; Wang, S.-G.; Yamauchi, Y.; Wu, K. C.-W. Controlling Particle Size and Structural Properties of Mesoporous Silica Nanoparticles Using the Taguchi Method. *J. Phys. Chem. C* **2011**, *115*, 13158−13165.

(47) Moulik, S. P.; Paul, B. K. Structure, Dynamics and Transport Properties of Microemulsions. *Adv. Colloid Interface Sci.* **1998**, *78*, 99−195.

(48) Matsumoto, S.; Sherman, P. The Viscosity of Microemulsions. *J. Colloid Interface Sci.* **1969**, *30*, 525−536.

(49) Qureshi, M.; Varshney, K. G. *Inorganic Ion Exchangers in Chemical Analysis*; CRC Press: Boca Raton, FL, 1991.

(50) Sing, K. S. W. Reporting Physisorption Data for Gas/Solid Systems. *Pure Appl. Chem.* **1982**, *54*, 2201−2218.

(51) Sakamoto, Y.; Kaneda, M.; Terasaki, O.; Zhao, D. Y.; Kim, J. M.; Stucky, G.; Shin, H. J.; Ryoo, R. Direct Imaging of the Pores and Cages of Three-Dimensional Mesoporous Materials. *Nature* **2000**, *408*, 449−453.

(52) Haag, W. O.; Lago, R. M.; Weisz, P. B. The Active Site of Acidic Aluminosilicate Catalysts. *Nature* **1984**, *309*, 589−591.

(53) Romero, A. A.; Alba, M. D.; Zhou, W.; Klinowski, J. Synthesis and Characterization of the Mesoporous Silicate Molecular Sieve MCM-48. *J. Phys. Chem. B* **1997**, *101*, 5294−5300.

(54) Handke, M.; Mozgawa, W. Vibrational Spectroscopy of the Amorphous Silicates. *Vib. Spectrosc.* **1993**, *5*, 75−84.

(55) Decottignies, M.; Phalippou, J.; Zarzycki, J. Synthesis of Glasses by Hot-Pressing of Gels. *J. Mater. Sci.* **1978**, *13*, 2605−2618.

(56) Takahashi, R.; Sato, S.; Sodesawa, T.; Kawakita, M.; Ogura, K. High Surface-Area Silica with Controlled Pore Size Prepared from Nanocomposite of Silica and Citric Acid. *J. Phys. Chem. B* **2000**, *104*, 12184−12191.

(57) Yu, K. M. K.; Thompsett, D.; Tsang, S. C. Ultra-Thin Porous Silica Coated Silver-Platinum Alloy Nano-Particle as a New Catalyst Precursor. *Chem. Commun. (Cambridge, U.K.)* **2003**, 1522−1523.

(58) Saniger, J. M. Al-O Infrared Vibrational Frequencies of γ-Alumina. *Mater. Lett.* **1995**, *22*, 109−113.

(59) Shen, J.; Cortright, R. D.; Chen, Y.; Dumesic, J. A. Microcalorimetric and Infrared Spectroscopic Studies of γ-Al_2O_3 Modified by Basic Metal Oxides. *J. Phys. Chem.* **1994**, *98*, 8067−8073.

(60) Gu, F. N.; Zhou, Y.; Wei, F.; Wang, Y.; Zhu, J. H. Creating the Adsorptive Sites with High Performance toward Nitrosamines in Mesoporous Silica MCM-41 by Alumina Modifier. *Microporous Mesoporous Mater.* **2009**, *126*, 143−151.

(61) Miller, F. A.; Wilkins, C. H. Infrared Spectra and Characteristic Frequencies of Inorganic Ions. *Anal. Chem.* **1952**, *24*, 1253−1294.

(62) Cheralathan, K. K.; Hayashi, T.; Ogura, M. Post-Synthesis Coating of Alumina on the Mesopore Walls of SBA-15 by Ammonia/Water Vapour Induced Internal Hydrolysis and its Consequences on Pore Structure and Acidity. *Microporous Mesoporous Mater.* **2008**, *116*, 406−415.

(63) Tarte, P. Infra-Red Spectra of Inorganic Aluminates and Characteristic Vibrational Frequencies of AlO_4 Tetrahedra and AlO_6 Octahedra. *Spectrochim. Acta* **1967**, *23A*, 2127−2143.

(64) Kwon, S. G.; Hyeon, T. Formation Mechanisms of Uniform Nanocrystals via Hot-Injection and Heat-Up Methods. *Small* **2011**, *7*, 2685−2702.

(65) Nakamura, T.; Mizutani, M.; Nozaki, H.; Suzuki, N.; Yano, K. Formation Mechanism for Monodispersed Mesoporous Silica Spheres and Its Application to the Synthesis of Core/Shell Particles. *J. Phys. Chem. C* **2007**, *111*, 1093−1100.

(66) Anderson, M. T.; Martin, J. E.; Odinek, J. G.; Newcomer, P. P. Surfactant-Templated Silica Mesophases Formed in Water: Cosolvent Mixtures. *Chem. Mater.* **1998**, *10*, 311−321.

(67) Wang, W.; Wang, S.; Ma, X.; Gong, J. Recent Advances in Catalytic Hydrogenation of Carbon Dioxide. *Chem. Soc. Rev.* **2011**, *40*, 3703−3727.

(68) Toyir, J.; de la Piscina, P. R.; Fierro, J. L. G.; Homs, N. Highly Effective Conversion of CO_2 to Methanol over Supported and Promoted Copper-Based Catalysts: Influence of Support and Promoter. *Appl. Catal., B* **2001**, *29*, 207−215.

(69) Behrens, M.; Studt, F.; Kasatkin, I.; Kühl, S.; Hävecker, M.; Abild-Pedersen, F.; Zander, S.; Girgsdies, F.; Kurr, P.; Kniep, B.-L.; Tovar, M.; Fischer, R. W.; Nørskov, J. K.; Schlögl, R. The Active Site of Methanol Synthesis over $Cu/ZnO/Al_2O_3$ Industrial Catalysts. *Science* **2012**, *336*, 893−897.

(70) Prieto, G.; Zečević, J.; Friedrich, H.; de Jong, K. P.; de Jongh, P. E. Towards Stable Catalysts by Controlling Collective Properties of Supported Metal Nanoparticles. *Nat. Mater.* **2013**, *12*, 34−39.